Received 00th January 20xx,
Accepted 00th January 20xx

DOI: 10.1039/x0xx00000x

www.rsc.org/

Reaction mechanisms for long life and ultra-high power rechargeable Zn ion batteries†

Yun Li,[a] Shanyu Wang,[a] James Salvador,[b] Jinpeng Wu,[c,d] Bo Liu,[e] Wanli Yang,[c] Jiong Yang,[e] Wenqing Zhang,[e] Jun Liu,[f] and Jihui Yang[a,*]

Rechargeable aqueous Zn-ion batteries (ZIBs) are very promising for large-scale grid energy storage applications owing to their low cost, environmentally benign constituents, excellent safety, and relatively high energy density.[1, 2] Their usage, however, is largely hampered by the fast capacity fade. The cycle stability seems to be highly rate-dependent,[3] which poses an additional challenge, but can also play a pivotal role in uncovering the reaction mechanisms. The complexity of the reactions has resulted in long-standing ambiguities of the chemical pathways of Zn/MnO_2 system, and has led to many controversies with regard to their nature. In this report, we present a combined experimental and theoretical study of Zn/MnO_2 cells. We found that both H^+/Zn^{2+} intercalation and conversion reactions occur at different voltages, and that the rapid capacity fading can clearly be ascribed to the rate-limiting and irreversible conversion reactions at a lower voltage. By avoiding the irreversible conversion reactions at ~ 1.26 V, we successfully demonstrate ultra-high power and long-life Zn/MnO_2 cells which, after 1000 cycles, maintain an energy density of ~ 231 Wh kg^{-1} and ~ 105 Wh kg^{-1} at a power density of ~ 4 kW kg^{-1} (9C, ~ 3.1 A g^{-1}) and ~ 15 kW kg^{-1} (30C, ~ 10.3 A g^{-1}), respectively. The excellent cycle stability and power capability are superior to most reported ZIBs or even some lithium-ion batteries. The results establish accurate electrochemical reaction mechanisms and kinetics for Zn/MnO_2, and identify the interplay of the voltage window and rate as the determining factors for achieving excellent cycle life.

Broader Context

The increasing interest and importance in large-scale grid storage technology are attributed to multiple factors, including managing peak demands, improving the grid reliability, integrating most sustainable energy sources such as solar radiation, wind, wave power, geothermal energy, etc., and further powering the energy infrastructures. Rechargeable aqueous Zn-ion batteries (ZIBs) with mild electrolytes have the advantages of low cost materials (Zn/MnO_2), manufacturing (air- and water-inert Zn anode), and recycling (mild electrolytes); relatively high energy density; and excellent safety, making them prospective candidates for large-scale grid storage. Their low cyclability, however, has remained a grand challenge, hindering the widespread applications of these attractive ZIBs. A prerequisite for improving the cycle life and electrochemical performance of Zn/MnO_2 batteries is to accurately determine the reaction mechanisms, especially under different rates, which poses a considerable challenge. In our combined experimental and computational study, a concomitant intercalation and conversion reactions of H^+/Zn^{2+} occurring at different voltages in the Zn/MnO_2 system is established. The rapid capacity fading is unambiguously ascribed to the rate-limiting and irreversible conversion reactions at a lower voltage. By mitigating or avoiding the irreversible conversion reactions at the lower voltage, we demonstrate high performance Zn/MnO_2 cells with ultrahigh power capability and excellent cycle life.

[a] *Material Science and Engineering Department, University of Washington, Seattle, WA 98195, USA.*
[b] *Chemical Sciences and Materials Systems Lab, General Motors R&D Center, Warren, Michigan 48090, USA.*
[c] *Advanced Light Source, Lawrence Berkeley National Laboratory, Berkeley, CA 94720, USA.*
[d] *Geballe Laboratory for Advanced Materials, Stanford University, Stanford, CA 94305, USA.*
[e] *Material Genome Institute, Shanghai University, 99 Shangda Road, Shanghai 200444, China.*
[f] *Energy & Environment Directorate, Pacific Northwest National Laboratory, Richland, WA 99352, USA.*
** Email: jihuiy@uw.edu*
†Electronic Supplementary Information (ESI) available: XRD spectra and XRF analysis of the electrodes; SEM of Zn anode; the Gibbs free energies of representative reactions. See DOI: 10.1039/x0xx00000x

Introduction

Large-scale grid storage technology is critical for managing peak demands, improving the grid reliability, integrating most sustainable energy sources such as solar radiation, wind, wave power, geothermal energy, etc., and further powering the energy infrastructures.[1, 2] In spite of the prosperous research on Li-ion and beyond Li-ion batteries with high energy

densities, many other factors including high-cost, safety, cycle life, and power capability, etc., will likely limit their use in stationary grid storage.[4-7] In fact for large-scale stationary grid storage, low cost, durability, and high-power capability for frequent peak clipping and valley filling usually outweigh the energy densities.[2, 8] Redox flow, sodium sulfur, and lead carbon chemistries have been proposed as alternative systems, but they also suffer from issues such as low rates, high operating temperatures, hazardous constituents, high costs, etc.[9-14] Low-cost aqueous batteries with earth abundant working ions, including Na^+ and Zn^{2+} are more promising.[15-23] Among these, aqueous ZIBs with mild electrolytes have the advantages of high energy density (~ 300 Wh kg^{-1}); low cost materials (*e.g.*, Zn/MnO_2), manufacturing (air- and water-inert Zn anode), and recycling (mild electrolytes); and excellent safety, making them prospective batteries for large-scale grid storage.[3, 21, 24-27]

The major limitation of aqueous Zn/MnO_2 for grid storage, however, is the poor cycle stability. Aqueous Zn/MnO_2 system is the prototypical primary alkaline batteries with KOH as the electrolyte.[28-30] A wide range of failure mechanisms largely prevents their effective use as the secondary batteries.[31-38] Recently, using nanostructured α-MnO_2 as the cathode active material, Xu et al. investigated the aqueous ZIB using $ZnSO_4$ as the electrolyte, demonstrating an intercalation reaction of Zn^{2+} into MnO_2 with good cycle stability and high energy density.[39] A similar study has been reported by Pan et al.,[3] yet a distinct conversion reaction involving protons in the cathodic reactions was suggested, analogous to the argument of Kim et al.[40] Despite significant prior efforts, phase transformation between different polymorphs, Mn dissolution, electrochemically inactive byproducts, use of $MnSO_4$ additive, low electronic conductivity, etc., still make it very challenging to improve cycle stability of the Zn/MnO_2 cells.[3, 39-49] For example, the selection of a MnO_2 polymorph with a larger tunnel size such as the todorokite-MnO_2 or the addition of $MnSO_4$ in the electrolyte to decrease the pH cannot completely solve the cycle life issues.[3, 40, 41] A necessity for improving the cycle life and electrochemical performance of Zn/MnO_2 batteries is the accurate determination of the reaction products and mechanisms, especially under different rates, which poses a grand challenge. On the experimental side, X-ray diffraction (XRD) data leave ambiguities due to the diffraction peaks overlapping and the low crystallinity for many possible reaction products.[38, 39, 45-47, 50] Nuclear magnetic resonance (NMR) or high resolution transmission electron microscopy offers localized structure, composition, and chemical environment information,[3, 45, 46] but macroscopic and quantitative analysis is difficult. In terms of the theoretical efforts, the computational modeling has been hindered by the complexity and a large variety of the reaction products (different phases and compositions) under various rates, which necessitates experimental guidance to reduce the required computational resources. Therefore, a coupled experimental and computational approach is called for to reveal the reaction mechanisms, clarify the origin of capacity fading, and design high performance ZIBs.

In this combined experimental and computational study, we unravel a concomitant intercalation and conversion reactions of H^+/Zn^{2+} occurring at different voltages in the Zn/MnO_2 system. The rapid capacity fading is unambiguously ascribed to the rate-limiting and irreversible conversion reactions at a lower voltage. The active MnO_2 cathode materials were electrodeposited *in-situ* from $MnSO_4$-based electrolyte onto the current collectors, inspired by the electrodeposition of electrolytic MnO_2 (EMD) used in the alkaline primary batteries.[51-55] By minimizing or avoiding the irreversible conversion reactions at the lower voltage, we demonstrated high performance Zn/MnO_2 cells which can deliver high energy and power densities of ~ 300 Wh kg^{-1} and ~ 2 kW kg^{-1} at 3C (1.032 A g^{-1}), ~ 231 Wh kg^{-1} and ~ 4 kW kg^{-1} at 9C (3.096 A g^{-1}), and ~ 105 Wh kg^{-1} and 15 kW kg^{-1} at 30C (10.32 A g^{-1}) with negligible capacity fading after 100 (at 3C), 1000 (at 9C), and 1000 (at 30C) cycles. These values are superior to most reported ZIBs or even some lithium-ion batteries. Furthermore, the revealed reaction mechanisms in our *in-situ* electrochemically deposited Zn/MnO_2 cells should be ubiquitous to those previously reported *ex-situ* Zn/MnO_2 cells or other ZIBs, and thus should be applicable for improving their cycle stability.

Experimental Section

Materials and characterization

The electrodes for *in-situ* deposited MnO_2 were prepared by thoroughly mixing 45 wt.% carbon black (TIMCAL Graphite & Carbon super P, MTI Corporation, USA) and 55 wt.% polyvinylidene fluoride (PVDF) in N-Methyl-2-pyrrolidone (NMP). The slurries made by a planetary centrifugal mixer (ARE-310, Thinky, USA) were cast on Ni foils by a MC-20 Mini-Coater (Hohsen, Japan). Ni foils with coatings were then dried in vacuum at 100 °C for 6 h to get rid of the NMP solvent.

Powder XRD data of the cathode materials were collected on a Rigaku RAPID II (Mo Kα radiation, Rigaku, Japan) between 5° and 45° (2θ) at room temperature. Microstructures of the samples were determined by a field emission scanning electron microscope (FESEM) equipped with Oxford energy dispersive spectroscopy (EDS) (FEI Sirion XL30, USA). The sample chemical compositions were determined by a 2D Micro-X-ray Fluorescence analyzer (Micro-XRF, M4 TORNADO, Bruker, USA). Inductively coupled plasma atomic emission spectroscopy (ICP-AES) was used to determine the mass loadings of MnO_2 deposits. To investigate the evolution of the Mn oxidation state in the electrodes, soft X-ray absorption spectroscopy (sXAS) data were collected in total electron yield mode in the iRIXS endstation at Beamline 8.0.1 of the Advanced Light Source at Lawrence Berkeley National Laboratory[Please cite RSI (2017) doi:10.1063/1.4977592 - all experimental specifications are provided there]. Experimental resolution of sXAS is about 0.15 eV without considering core hole lifetime broadening. For *ex-situ* XRD, sXAS, SEM, and XRF studies, the recovered electrodes after electrochemical cycling were rinsed with deionized water and dried at room temperature.

Electrochemical test

Electrochemical tests were carried out in both coin cells and three-electrode open cells. The cathodes were assembled in 2032 type coin cells with selected electrolytes and 0.5 mm thick excess Zn foil as the anodes. Glass fiber membrane filters (Whatman) were used as the separators. In the three-electrode open cells, the cathodes were used as the working electrodes, and Zn foils as the reference electrodes and the counter electrodes. The coin cells and the three-electrode open cells were cycled galvanostatically between 1.0 and 1.8 V (vs. Zn^{2+}/Zn) at 30 °C using a multifunction model 4200 battery tester (Maccor, USA). Cyclic voltammetry (CV) tests were carried out using a Reference 600 Potentiostat (Gamry, USA) at a scan rate between 0.1 and 1.0 mV s^{-1}. In the CV cells, the cathodes were used as the working electrode, silver chloride electrodes as the reference electrodes, and Pt foil the counter electrodes. The electrolytes used were 0.2 M $MnSO_4$+1 M $ZnSO_4$ aqueous solutions.[3] Electrochemical impedance spectroscopy (EIS) tests were carried out using a VersaSTAT 4 potentiostat (Ametec Scientific Instruments, USA) with a frequency range from 1 MHz to 0.01 Hz and an AC amplitude of 5 mV.

First-principles calculations

All calculations in the present study were performed within the generalized gradient approximation (GGA) using the Perdew, Burke and Ernzerhof (PBE) exchange–correlation functional.[56] A planewave basis set and the projector augmented wave (PAW) method as implemented in the Vienna Ab initio Simulation Package (VASP) were used,[57-60] based on the density functional theory (DFT). Furthermore, to account for the strong onsite Coulombic repulsion of the Mn-3*d* electrons, the GGA+U method was used for the Mn-containing compounds.[61] The effective onsite Coulombic term U_{eff} of the Mn-3d electrons was chosen to be 3.9 eV, according to a previous reference.[62] Zn-doped MnO_2 calculations were performed in fully relaxed 2×2×1 supercells. The Monkhorst–Pack scheme 5×5×2 k-point sampling was used for the integration in the irreducible Brillouin zone.[63] The cutoff energy for the plane waves is set to be 520 eV. The total ground state energy converged within 10^{-5} eV. The lattice parameters and the ionic position were fully relaxed, and the final forces on all atoms were less than 0.01 eV/Å.

Results and discussion

Electrochemical performance of *in-situ* deposited Zn/MnO_2 cells

Carbon black was used as the MnO_2 cathode electrodeposition substrate due to its high electrical conductivity, porous structure, and large surface area; all of which are beneficial for the electrodeposition and the subsequent electrochemical reactions. To evaluate the energy storage capability of the in-situ Zn|$MnSO_4$, $ZnSO_4$|carbon-black cells, the coin cells were tested in the potential range of 1.0-1.8 V vs. Zn^{2+}/Zn (Fig. 1). Fig. 1a shows the initial electrodeposition of MnO_2 cathode at a current density of 0.01 mA cm^{-2} for 30 h and the subsequent galvanostatic discharge/charge profiles of the cell at a current density of C/3 (C = 0.344 A g^{-1}). The typical loading of MnO_2 deposits is ~ 0.54 mg cm^{-2} based on the electrodeposition charge, which is approximately consistent with the average loading of ~ 0.47 mg cm^{-2} derived from the ICP measurements. The initial electrodeposition plateau is at ~ 1.73 V vs. Zn^{2+}/Zn and the two discharge plateaus are at ~ 1.40 V and ~ 1.26 V. On the subsequent cycles, new charge plateaus appear at ~ 1.51 V and ~ 1.58 V. The charge/discharge plateau potentials are in good agreement with the CV redox peaks shown below, as will be discussed later. The appearance of 1.40/1.26 V discharge and 1.58/1.51 V charge plateaus was also observed in previous reports, which were assigned as either Zn-intercalation or proton-conversion reactions associated with the crystallographic evolution of MnO_2 during the cycling processes.[3, 40, 41, 46-49] In this work, we will show that the two discharge plateaus at 1.40 V and 1.26 V represent more complicated reactions which incorporate both H^+ and Zn^{2+} into the MnO_2 host and reducing Mn(4+) into Mn(3+)/Mn(2+).

The cycling performance at the C/3 rate is shown in Fig. 1b. The capacity increase in the first few cycles is due to a gradual activation of the deposited MnO_2 (electrolyte wetting, surface stabilization, etc.). After the activation, the cell suffers severe capacity fading from 400 to 20 mAh g^{-1} within 100 cycles. The poor cycle stability leads us to speculate that there may exist irreversible reactions (*e.g.*, conversion reaction or other side reactions) during discharge that cause significant disruption of the original electrode architecture or material crystal structures. Interestingly, the capacity retentions are significantly better at higher discharge/charge rates, as shown in Fig. 1b, *e.g.*, ~ 30% and ~ 80% discharge capacity retentions at 1C and 3C after 100 cycles, respectively. This electrochemical behavior is related to the unique reaction mechanisms in Zn/MnO_2, which will be discussed below.

Figure 1c shows the initial discharge/charge profiles of the Zn/MnO_2 cells at C/3, 1C, and 3C. The cells cycled at higher rates (1C and 3C) show lower discharge and charge capacities as expected. Upon close examination of the discharge plateaus, we find that the first discharge plateau at ~ 1.40 V shows comparable specific capacities among different rates (~ 175 mAh g^{-1} for 3C and ~ 210 mAh g^{-1} for C/3), while the capacity pertaining to the second discharge plateau at ~ 1.26 V decreases significantly from ~ 190 mAh g^{-1} at C/3 to ~ 100 mAh g^{-1} at 3C. This clearly indicates that these two plateaus have distinctive rate-dependent kinetics, such that the electrochemical reactions at 1.26 V are kinetically limited at high rates, while those at 1.40 V are only slightly dependent on the rate. The capacity retention data are plotted in Fig. 1d, as such, the discharge/charge profiles for the 100th cycle at the 3C rate show that the cell retains ~ 90% and ~ 60% of the discharge capacity of the 1.40 V and 1.26 V plateaus, respectively. The cell cycled at the 1C rate, however, mostly

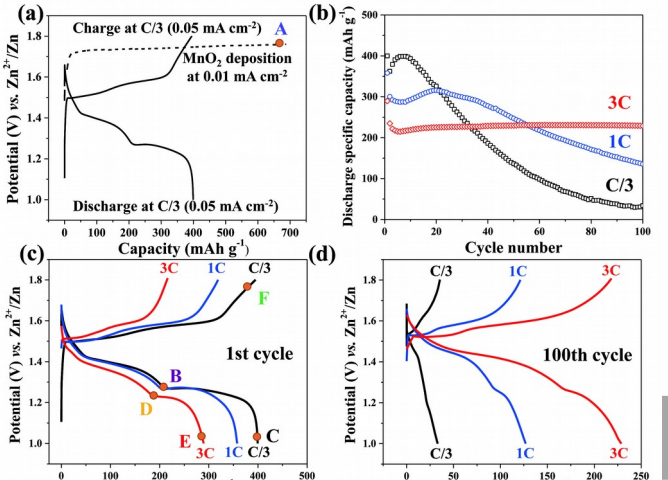

displays capacity corresponding to the 1.40 V discharge plateau after 100 cycles. Therefore, these data seem to suggest that the high capacity retention at high rates is mainly due to the reversible reactions occurring at the ~ 1.40 V discharge plateau as well as the significantly kinetically-limited irreversible reactions at 1.26 V. At high rates, the irreversible reactions are greatly suppressed and hence better capacity retention is achieved. The poor capacity retention for the cell cycled at the C/3 rate should be attributed to the irreversible reactions occurring at ~ 1.26 V. These irreversible reactions (primarily conversion reactions) bring about massive inactive products and substantial structural stresses originated from drastic phase transitions that severely disrupt cathode structure and thus block the ion and electron transport, resulting in ~ 80% and ~ 90% capacity losses at ~ 1.40 V and ~ 1.26 V, respectively.

Redox reaction mechanisms

XRD and XRF To elucidate the reaction mechanisms in the *in-situ* Zn/MnO_2 cells, structure and composition of the *in-situ* formed MnO_2 cathode and its evolution during discharge/charge were examined by *ex-situ* XRD. The XRD patterns were carefully collected for the original MnO_2 deposits (labeled as A in Fig. 1a and shown in Fig. 2), cathode after fully discharged at C/3 (labeled as C in Fig. 1c and shown in Fig. 2a),

and after fully discharged at 3C (labeled as E in Fig. 1c and shown in Fig. 2b). The originally deposited MnO_2 cathode (A, Fig. 2) can be indexed to the hexagonal structure of birnessite δ-MnO_2 (JCPDS 18-0802), which can also be viewed as a layered MnO_2. Crystal structure of the hexagonal birnessite δ-MnO_2 consists of sheets of edge-sharing $[Mn^{4+/3+}O_6]$ octahedra with some Mn vacancies, and interlayer $[Mn^{3+/2+}O_6]$ octahedra located above/below in-sheet Mn vacancies.[64-66] The charge of in-sheet Mn vacancies is compensated by the interlayer $Mn^{3+/2+}$ or other cations such as Zn^{2+} and H^+. Compared with the originally deposited MnO_2, the diffraction patterns of MnO_2 cathodes discharged to 1.0 V at C/3 (C) and 3C (E) shift ~ 0.5° (2θ) towards lower angles. This clearly indicates a lattice expansion caused by cation insertion, such as H^+/Zn^{2+} intercalation.[31, 46, 48, 49] Meanwhile, some characteristic peaks of MnOOH (JCPD #01-075-1199) appear, presumably formed during the H^+ insertion accompanied by a structural relaxation (*e.g.*, vacancy redistribution and/or rearrangement of Mn-O bonds).[33, 38, 67, 68] The same peak shift and the appearance of MnOOH for both points C and E suggest similar H^+/Zn^{2+} intercalation processes at high (3C) and low (C/3) rates. Furthermore, similar peak shift of MnO_2 and appearance of MnOOH for cathodes discharged to 1.3 V at C/3 (point B for the 10th cycle in Figs. 1c and 2a) and 3C (point D for the 10th cycle in Figs. 1c and 2b) after 10 cycles suggest that the H^+/Zn^{2+} intercalation processes occurring prior to 1.3 V (at 1.40 V).

After fully discharged to 1.0 V at C/3 (Fig. 2a), the XRD of point C clearly shows the formation of massive basic zinc sulfate $ZnSO_4{\cdot}3Zn(OH)_2{\cdot}nH_2O$ (mainly n = 4 with JCPDS # 09-0204), in addition to the H^+/Zn^{2+}-inserted MnO_2 phases. Additionally, new diffraction peaks appear at 26.1° (2θ), 36.2° (2θ), 37.6° (2θ), which can be indexed to be Mn_3O_4 (JCPDS # 24-0734), while the 26.1° (2θ) peak can also be assigned to MnO (JCPDS # 01-1206). The appearance of $ZnSO_4{\cdot}3Zn(OH)_2{\cdot}nH_2O$, Mn_3O_4, and MnO after fully discharge is in good agreement with our hypothesis of conversion reactions at 1.26 V. In addition, the

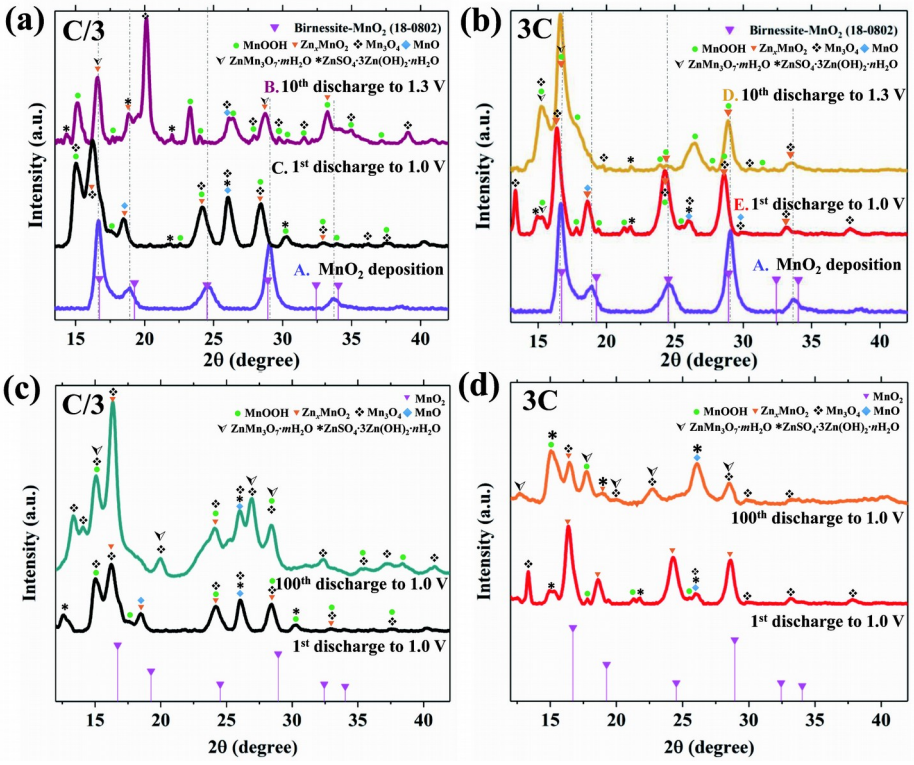

Fig. 2 Comparison of XRD patterns of initially deposited MnO_2, partially, and fully discharged cathodes at current densities of (a) C/3 and (b) 3C. XRD patterns of fully discharged cathodes after 1st and 100th cycles at (c) C/3 and (d) 3C.

XRD pattern of the fully charged state (F in Fig. 1c and Fig. S1a, ESI†) is quite similar to that of the originally deposited MnO_2 electrode (A), implying that the parent MnO_2 phase is largely recovered after the initial recharge. The long-term cycling at low rates, however, will irreversibly accumulate Mn_3O_4 and $ZnSO_4{\cdot}3Zn(OH)_2{\cdot}nH_2O$ from the conversion reactions, evident by the apparent diffraction peak of Mn_3O_4 at 20.1° in the XRD of point B for the 10th cycle. After 100 cycles (Fig. 2c), the irreversible conversion products Mn_3O_4, MnO, and $ZnSO_4{\cdot}3Zn(OH)_2{\cdot}nH_2O$ predominate on the electrodes, eventually disrupt the electrode structure and result in a poor capacity retention, as will be discussed in more details below.

XRD of the cathode discharged to 1.0 V at a high rate of 3C (point E) is shown in Fig. 2b. The apparent lower peak intensities of $ZnSO_4{\cdot}3Zn(OH)_2{\cdot}nH_2O$, Mn_3O_4, and MnO for fully-discharged cathode (point E) and partially-discharged cathode after 10 cycles (point D) suggest a significant suppression of the conversion reactions occurring at 1.26 V, well consistent with the largely decreased capacity of the second discharge plateau at the 3C rate. The Zn^{2+} conversion phase $ZnMn_3O_7{\cdot}mH_2O$ only shows as a weak peak at 2θ of 15.4° (Fig. 2b) in the initial discharge processes, however, intensified peaks of $ZnMn_3O_7{\cdot}mH_2O$ were identified after 100 cycles. Fig. 2d compares the XRD patterns of fully-discharged electrodes at 3C after the 1st and 100th cycles. The original H^+/Zn^{2+}-inserted MnO_2 phases nearly disappear after 100 cycles. Instead, conversion products $ZnMn_3O_7{\cdot}mH_2O$, tunneled Zn-woodruffite [T(3, 4)] (JCPDS # 47-1825), and Mn_3O_4 dominate after 100 cycles.

As shown in Fig. 2, the diffraction peaks overlap for many discharged products. Meanwhile, some discharge products are mutually transformable through various intermediate phases depending on the local pH value, humidity, temperature, etc.[50, 69, 70] Therefore, it is very challenging to exactly distinguish the phases in the electrode via XRD only, but the XRD results are insightful to unravel the trend of phase transition from MnO_2 to MnOOH and Zn_xMnO_2, and finally to Zn^{2+}/H^+ conversion products, more significantly to clarify the origin of capacity fade.

XRF analyses results of the cathodes at different stages of the first discharge/charge are shown in Fig. S1b (ESI†). The signals of Zn and S are normalized to the Mn signal. The initially deposited cathode is mainly composed of Mn as expected (O is not resolved here), with a slight $ZnSO_4$ contamination from the electrolyte. The Zn and S contents, predominantly from Zn_xMnO_2, $ZnSO_4{\cdot}3Zn(OH)_2{\cdot}nH_2O$, and $ZnMn_3O_7{\cdot}mH_2O$, increase significantly for the fully discharged cathodes, and nearly revert to the original values after recharging, indicating the almost reversible electrochemical processes in the first discharge/charge. The cathode discharged at C/3 shows a doubled Zn content and almost a quadrupled S content compared to those discharged at 3C, which are consistent with their distinct discharged capacities (~ 400 mAh g^{-1} *vs.* ~ 290 mAh g^{-1}). More specifically, based on the high Zn content of discharged cathode at 3C we can confirm the existence of Zn^{2+}-incorporated products, since at least 11% Zn (of the overall 39% Zn) in the cathode comes from Zn_xMnO_2 or $ZnMn_3O_7{\cdot}mH_2O$ while the rest (28% Zn based on 7% S) is from $ZnSO_4{\cdot}3Zn(OH)_2{\cdot}nH_2O$.

sXAS In order to directly detect the chemical states of Mn, Mn *L*-edge sXAS was performed on electrodes at the representative electrochemical stages, as shown in Fig. 3. Compared with the hard X-ray XAS of Mn K-edge that has been extensively applied to study the valence of Mn in rechargeable Zn/MnO_2 c ells,[46, 48] soft X-ray based sXAS is a more direct and sensitive probe to determine the valence 3d states of transition-metals (TMs) through the dipole-allowed *2p-3d* transitions[Please **add** citation: Chem Rev (2017) doi:10.1021/acs.chemrev.7b00007]. For TM oxide based battery materials, TM L-edge sXAS has been demonstrated as a sensitive and quantitative technique for fingerprinting the formal valence of the TM redox center.[71] [Please ***DELETE Ref#71 & Ref#72, REPLACE*** here with JPD (2016) doi: 10.1088/0022-3727/49/41/413003][72] Because TM-L sXAS probes the localized *3d* states directly, the Mn *L*-edge sXAS spectral lineshape is insensitive to specific structural differences, if a local octahedral structure is maintained.[73] The spectroscopic features could be well interpreted by comparing with reference spectra of different Mn states,[74] as indicated in Fig. 3 by the vertical dashed lines.

~~The absorption spectra of the Mn *L*-edge consist of well-separated features in two regions, L_3 (638-646 eV) and L_2 (649-~~

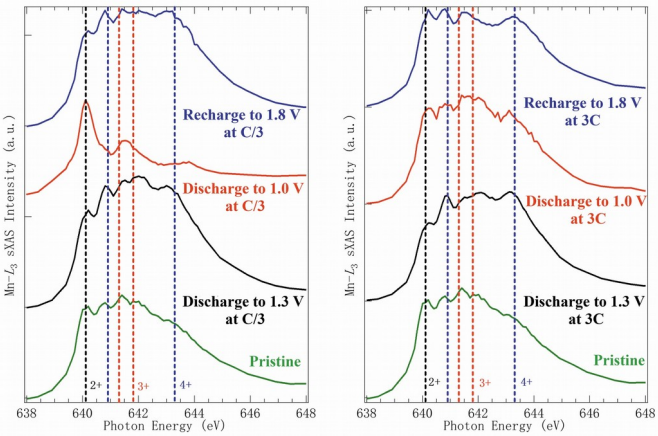

Fig. 3 Mn *L*-edge sXAS of initially deposited MnO_2, partially, and fully discharged and fully recharged cathodes at current densities of (a) C/3 and (b) 3C.

~~656 eV), due to the 2*p* core hole spin-orbital splitting~~ [If we mention this, we should at least show the full energy range Mn-L sXAS at least in Supplementary (I think we do have the data)!]. Fig. 3 focuses on Mn L_3-edge features that is much sharper compared with L_2 lineshape due to the intrinsic Coster-Kronig broadening. The spectra show that the as-deposited MnO_2 electrode (labeled as A in Fig. 1-3) contains Mn^{4+} (641 and 643.5 eV), Mn^{3+}(641.5 and 642 eV), and Mn^{2+} (640 eV), supporting the existence of birnessite δ-MnO_2 composed of $[Mn^{4+/3+}O_6]$ and $[Mn^{3+/2+}O_6]$ octahedral, as well as interlayer $Mn^{3+/2+}$ ions. The MnO_2 electrodes partially-discharged to 1.3 V retain the $Mn^{4+/3+/2+}$ mixture at both low (C/3, labeled as B in Fig. 1c and shown in Fig. 3a) and high (3C, labeled as D in Fig. 1c and shown in Fig. 3b) rates. It is consistent with the XRD results that show the current density (C-rate) has a minor effect on the H^+/Zn^{2+} intercalation reactions at ~ 1.40 V and thus similar H^+/Zn^{2+}-inserted δ-MnO_2 phases appear at C/3 and 3C. However, a striking sXAS contrast between different rates is clearly seen when the electrodes are fully discharged to 1.0 V. Mn^{2+} peak dominates the sXAS lineshape of the electrode at C/3 (labeled as C in Fig. 1c and shown in Fig. 3a), while Mn^{3+} and Mn^{2+} peak intensities only moderately increase with the 3C samples (labeled as E in Fig. 1c and shown in Fig. 3b). This result clearly reveals an almost complete reduction of $Mn^{4+/3+}$ to Mn^{2+} after fully discharge at C/3, accounting for the comparable discharge capacity of 190 mAh g^{-1} at 1.26 V reactions to that of 1.40 V reactions (210 mAh g^{-1}). For electrodes cycled with high rates (e.g., 3C), the kinetic-limited conversion reactions at 1.26 V are largely suppressed, resulting in a slight evolution of the Mn valences, and thus smaller contribution to the overall discharge capacity. The intensity of Mn^{4+} peaks recovers and becomes stronger when fully recharged, illuminating reversible Mn valence changes between Mn^{4+} and $Mn^{3+/2+}$. The stronger Mn^{4+} peaks in the recharged cathode might correspond to the activation of MnO_2 deposits in the first few cycles.,The finite amount of intensity variation here is likely a surface effect from the surface/bulk charge redistribution in the ex-situ samples and the limited sXAS probe depth of about 10 nm.[Delete Ref#75 here][75] Therefore, the sXAS results not only present the overall Mn valence evolution upon electrochemical potentials, they also reveal directly the sharp contrast on the 1.26 V discharge plateau in electrodes cycled at different rates.

SEM Figure 4 shows the surface morphology of the cathode at various cycling stages. The morphology of the originally deposited MnO_2 on carbon black surface shows hydrangea-shape clusters with several micrometers in diameter and petal-like nanosheets with thicknesses of tens of nanometers (Fig. 4a). After being discharged to 1.3 V at C/3 or 3C (Fig. 4b and 4e), the electrodes roughly retain the original morphology of the MnO_2 clusters, primarily due to the intercalation reactions occurring at 1.40 V. For the fully discharged cathode (1.0 V at C/3), however, large flakes with sizes of ~ 10-20 μm, as shown in Fig. 4c, can be identified to be $ZnSO_4{\cdot}3Zn(OH)_2{\cdot}nH_2O$ by means of EDS. These flakes, covering and growing across the MnO_2 clusters, would block the ion diffusion, disrupt the cathode structure, and thus result in a serious capacity loss in prolonged cycling. In contrast, for the cathode discharged at 3C, as shown in Fig. 4f, the intergrowth between MnO_2 nanosheets and $ZnSO_4{\cdot}3Zn(OH)_2{\cdot}nH_2O$ flakes provides a stable and percolating microstructure, which is beneficial for the electrochemical reactions. Moreover, the sizes of $ZnSO_4{\cdot}3Zn(OH)_2{\cdot}nH_2O$ flakes in 3C discharged electrode are less than 2 μm and they apparently present in smaller amounts than those discharged at low rates. For the charged cathode shown in Fig. 4d, the electrode reverts to the morphology of the original MnO_2 electrode, and only few $ZnSO_4{\cdot}3Zn(OH)_2{\cdot}nH_2O$ flakes are observed. The petal-shaped MnO_2 nanosheets are retained during the whole electrochemical reaction processes, implying a stable and reversible microstructure for the concurrent intercalation and conversion reactions in the first few cycles. This also agrees well with the reversible behavior in the XRD results.

In addition, the high reversibility of the Zn anode also contributes to the good cycling performance. SEM images of Zn anodes before and after 20 cycles are shown in Fig. S2 (ESI†). The laminated Zn was well deposited with no sign of Mn contamination and no significant surface oxidation (EDS).

Summary of the reaction mechanism and DFT simulations

Based on the above experimental analyses of electrochemical behavior, XRD, XRF, sXAS, and SEM, we can summarize the redox reactions and structural transformations occurring in the *in-situ* Zn/MnO_2 cell, as shown in Fig. 5. To further confirm our proposed reaction pathway, we employed DFT simulations to calculate the voltages of the two redox reactions occurring at ~ 1.40 V and ~ 1.26 V. Our calculations considered various H^+/Zn^{2+} intercalation and conversion reactions with MnO_2. The voltage of a redox reaction can be obtained from the difference in the total Gibbs free energy between the products and reactants, and the Gibbs free energies and structures of all compounds were computed based on fully relaxed structures. Based on the DFT results, the major redox reactions can be formulated as below

1). H^+/Zn^{2+} intercalation reactions at ~ 1.40 V

$$84MnO_2 + 33Zn + 10ZnSO_4 + 100H_2O \rightleftharpoons H^+/Zn^{2+} \quad (1)$$

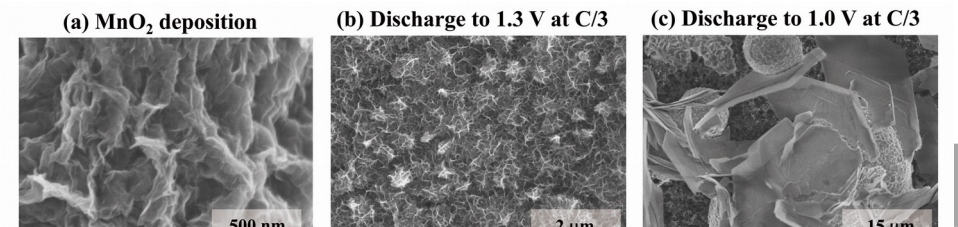

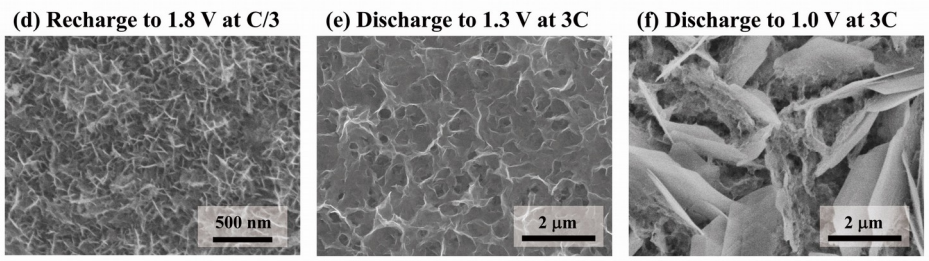

Fig. 4 SEM images of the cathode recovered from the test cells after (a) MnO_2 deposition, discharged to (b) 1.3 V and (c) 1.0 V at C/3, (d) fully charged at C/3, and discharged to (e) 1.3 V and (f) 1.0 V at 3C.

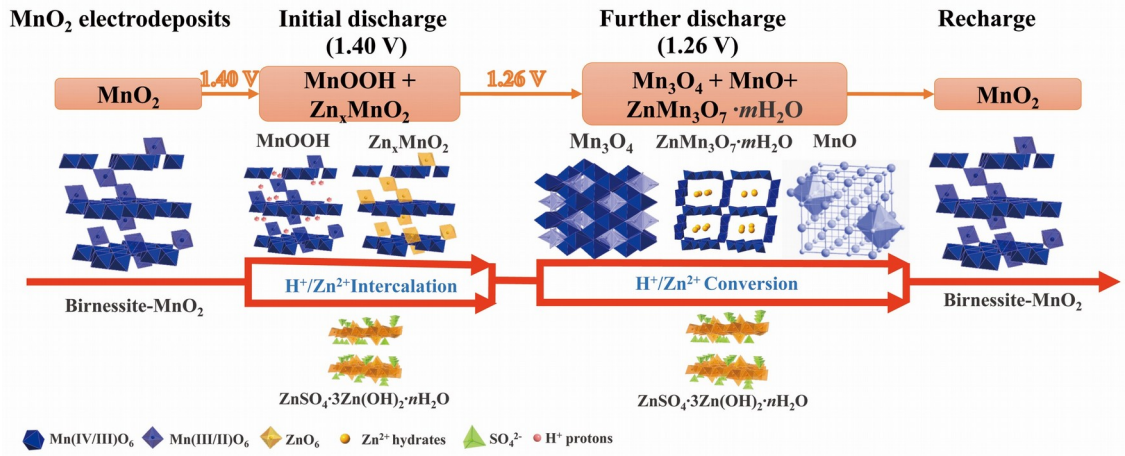

Fig. 5 Schematic illustration of the redox reactions and crystal structures of related compounds in the Zn|0.2M $MnSO_4$ (aq), 1M $ZnSO_4$ (aq)|carbon black cells.

2). H^+/Zn^{2+} conversion reactions at ~ 1.26 V

$$8\,Zn_{0.125}MnO_2 + 16MnOOH + 4Zn + ZnSO_4 + 3H_2 \quad . \quad 2$$

The calculated voltages for Equations (1) and (2) are 1.39 V and 1.26 V and agree very well with the experimental results. Here we took $Zn_{0.125}MnO_2$ as the Zn-insertion compound for simplicity, and MnOOH as the H^+-insertion compound. We also

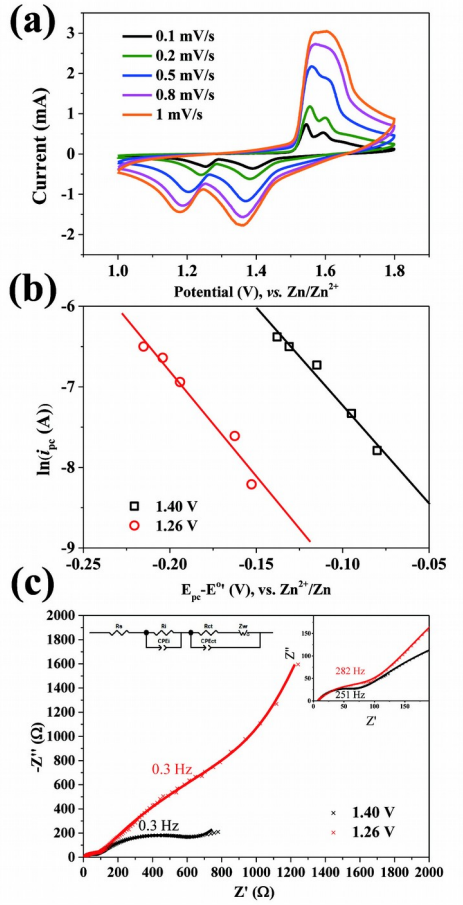

Fig. 6 (a) Cyclic voltammograms of *in-situ* deposited MnO_2 cathode at various scan rates (0.1, 0.2, 0.5, 0.8, 1.0 mV s^{-1}). (b) Plots of ln i_{pc} *vs.* (E_{pc}-$E^{o\prime}$) for the 1.40 V and 1.26 V reductions. (c) EIS analysis of MnO_2 cathode discharged to 1.40 V and 1.26 V.

calculated the voltages of other possible redox reactions, such as Zn^{2+} intercalation as the exclusive reaction at the initial discharge stage, however, the calculated voltages are significantly different from the experimental values which oblige us to rule out these scenarios, as shown in Table S1 (ESI†). The combined experimental and theoretical evidence ascertain the main reactions pathway in our *in-situ* Zn/MnO_2 cell, as illustrated in Fig. 5 and formulated in Equations (1)-(2). Due to the complexity of Zn/MnO_2 system, there might be some minor side reactions, which will not significantly contribute to the capacity and influence the electrochemical behavior.

Kinetic behaviours

To discern the different kinetic behavior of the two separate redox reactions at 1.40 V and 1.26 V, the standard reaction rate constants $k°_{1.40V}$ and $k°_{1.26V}$ were derived by CV and are shown in Fig. 6. Fig. 6a shows a series of cyclic voltammograms obtained at different scan rates (0.1-1 mV/s). It is clear that the reaction at 1.40 V is more reversible than the one at 1.26 V, due to its smaller peak separations (160-280 mV vs. 300-420 mV). The peak current is expressed as[76]

$$i_{pc} = 0.227nFACk^{o}\exp[-\frac{(\alpha n_a F)}{(RT)}(E_{pc} - E^{o'})] \quad (3)$$

where i_{pc} is the peak cathodic current; n the number of electrons involved in the overall electrode processes; A electrode area; C the maximum concentration change of H^+/Zn^{2+} in the cathode materials; α the charge transfer coefficient; n_a the number of electrons involved in the redox steps; E_{pc} the peak cathodic potential; and $E°'$ the formal potential. The average formal potential values of 1.48 V and 1.40 V are used to plot the ln i_{pc} *vs.* (E_{pc} - $E°'$) relations for the two reactions at 1.40 V and 1.26 V, respectively. Fig. 6b presents the plots of ln i_{pc} *vs.* (E_{pc} - $E°'$) obtained from the cyclic voltammograms in Fig. 6a. From the intercepts of the straight lines, the standard reaction rate constants $k°_{1.40V}$ and $k°_{1.26V}$ are calculated as 1.26×10^{-7} and 1.58×10^{-8} cm s^{-1}, respectively. The standard reaction rate constant at 1.40 V ($k°_{1.40V}$) is almost one order of magnitude larger than that at 1.26 V ($k°_{1.26V}$). $k°_{1.40V}$ is also comparable to that of $LiNi_{1/3}Co_{1/3}Mn_{1/3}O_2$ (NMC111) in Li-ion batteries for intercalation reaction (~ 2.5×10^{-7} cm s^{-1}).[77] The kinetic behavior was also studied by EIS. Fig. 6c shows the EIS results of a Zn/MnO_2 cell discharged to two different statuses (1.40 V and 1.26 V). The discharged cell displays two semicircles in high and middle frequency regions, representing the interfacial and charge transfer resistances, respectively, and a diffusion tail in low frequency region due to the ion-diffusion processes in solids.[43, 44] The EIS data can be well fitted using the equivalent circuit shown in the inset. After being discharged to 1.3 V at C/3, fitting the EIS data gives an internal resistance ($R_{s,1.40V}$, 7.3 Ω), an interfacial resistance ($R_{i,1.40V}$, 66.3 Ω), and a charge transfer resistance ($R_{ct,1.40V}$, 646.5 Ω). In comparison, the cell fully discharged to 1.0 V at C/3 shows a much higher $R_{ct,1.26V}$ (2019.2 Ω) but similar $R_{s,1.26V}$ (6.6 Ω) and $R_{i,1.26V}$ (93.2 Ω). The largely increased charge transfer resistance is primarily due to the irreversible conversion products, which disrupt the electrode structure and thus largely hinder the ion and electron transport, well consistent with above XRD and SEM analyses.

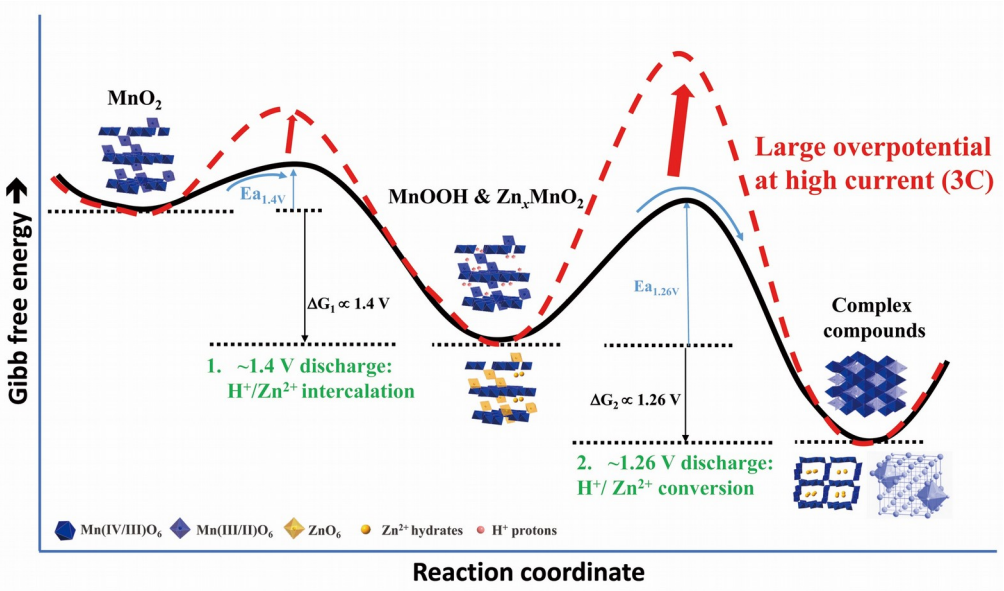

Fig. 7 Gibbs free energy *vs.* reaction coordinate showing the thermodynamic and kinetic properties of the redox reactions in Zn/MnO_2 cells with different rates.

In general, a kinetic-limited reaction has a small $k°$, a small exchange current density i_0, and thus a high R_{ct}. Thereby a large current density will require a high activation energy E_a and a large overpotential to allow the reaction to proceed at such a high rate. In this case, only a small fraction of the initial reactants has sufficient energy to overcome the energy barrier and form the final products, leading to a small measurable capacity. To illustrate the different kinetic behavior of the two redox reactions, reaction energetics are plotted in Fig. 7. For the H^+/Zn^{2+} intercalation reactions at ~ 1.40 V, a small energy barrier will allow for a large reaction rate, and an increase in

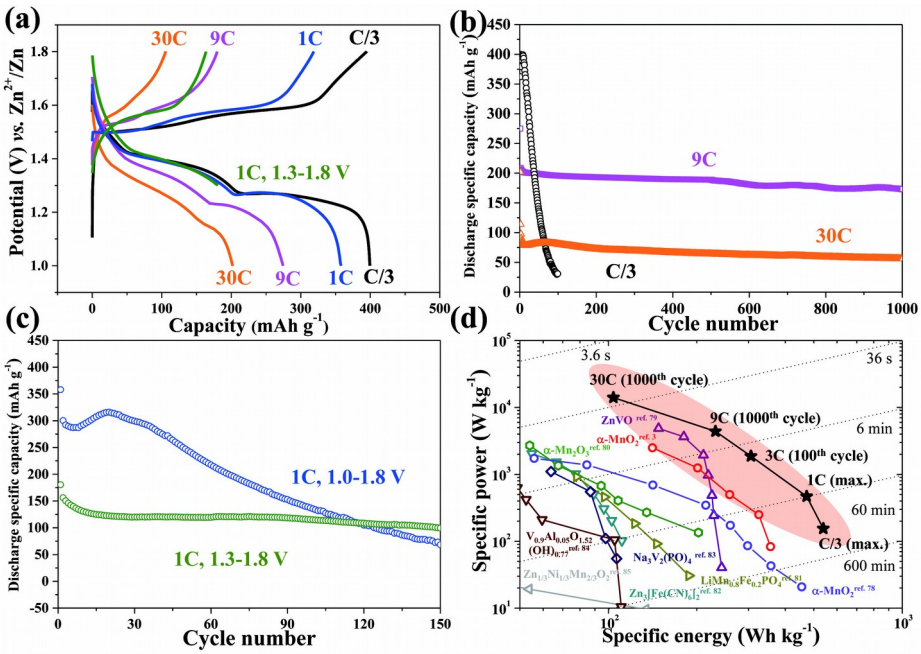

Fig. 8 (a) The discharge/charge profiles and (b,c) cycling performance of *in-situ* Zn/MnO_2 cells at different current densities (C/3, 9C, and 30C) and different voltage ranges (1.0-1.8V and 1.3-1.8 V). (d) Ragone plot (power vs energy densities) of the *in-situ* Zn/MnO_2 cells as compared with previously reported ZIBs with *ex-situ* MnO_2 and other cathode materials.

current will not significantly increase the energy barrier due to its large $k°_{1.40V}$ and low $R_{ct,1.40V}$. Furthermore, at 1.26 V, however, the rate-limiting process possesses a high activation barrier due to its small $k°_{1.26V}$ and high $R_{ct,1.26V}$, especially at high rates. The concurrence of conversion reactions with both H^+ and Zn^{2+} at 1.26 V is responsible for the undesirable rate performance, since these conversion reactions cause large volume change, sluggish phase transformation, the formation of electrochemically inactive $ZnSO_4{\cdot}3Zn(OH)_2{\cdot}nH_2O$, *etc.* Therefore, at large current densities, the slow conversion reactions will be largely suppressed, causing a capacity reduction but significantly improving overall capacity retention. Even though the reaction mechanisms demonstrated here is for our *in-situ* formed Zn/MnO_2 cells, we believe the concomitant intercalation and conversion reactions of H^+/Zn^{2+} could be ubiquitous in other aqueous Zn/MnO_2, considering the similar electrochemical behavior (discharge profiles, cycling properties) and similar cell structure (same electrodes and electrolytes).[3, 44, 47]

Optimizing the power capability and cycling stability

According to our understanding of the reaction mechanisms and kinetic behavior in Zn/MnO_2 cells, to improve the cycle stability it is desirable to mitigate/eliminate the rate-limiting, irreversible, and electrode-disrupting conversion reactions occurring at ~ 1.26 V. Since fast H^+/Zn^{2+} intercalation reactions are not influenced by the current density, mitigation/elimination of the conversion reactions could also largely improve the power density of the Zn/MnO_2 cell. As the first example, the *in-situ* Zn/MnO_2 cells were designed to be cycled at higher rates, *e.g.*, 9C and 30C, to restrain the irreversible H^+/Zn^{2+} conversion reactions at ~ 1.26 V, as shown in Fig. 8a-b. As expected, higher current density largely restrains the capacity of the second discharge plateau as compared to the discharge/charge profiles at C/3 (Fig. 8a). Consequently, as shown in the Fig. 8b, high rate cycling between 1.0 and 1.8 V largely improves the cycle stability. For instance, the 9C and 30C cell delivers a discharge capacity of 175 mAh g^{-1} and 75 mAh g^{-1} after 1000 cycles, respectively. More importantly, there is no significant capacity fading for the two cells after several initial cycles (to stabilize the cathode). Similarly, in a second example, by increasing the low cut-off voltage from 1.0 V to 1.3 V, the irreversible conversion reactions at 1.26 V can be avoided (Fig. 8a). The cell displays an initial capacity of 175 mAh g^{-1} at 1C, about half of that of the cell discharged to 1.0 V. After a rapid capacity fade in the initial 10 cycles, the cell discharged to 1.3 V shows a negligible capacity fading after 150 cycles, as shown in Fig. 8c. The reason for the large initial capacity drop in the cells at different current densities, as shown in Fig. 1 and 8, is unclear and will be investigated in the future.

Figure 8d shows the Ragone plot (power density vs. energy density) of *in-situ* Zn/MnO_2 cells as compared to previously reported Zn/MnO_2 cells and ZIBs with other cathode materials. Our cell cycled at 9C exhibits gravimetric energy and power

densities up to 231 Wh kg^{-1} and 4 kW kg^{-1}, respectively. These values, achieved after 1000 cycles, are much higher than those of conventional Zn/MnO_2 and ZIBs with other cathode materials published recently.[3, 78-85] In particular, the cell cycled at 30C demonstrates a power density of 15 kW kg^{-1}, close to those of supercapacitors.[86] Overall our *in-situ* aqueous Zn/MnO_2 cells show very competitive electrochemical performance suitable for stationary grid storage, especially taking into account their low cost and superior safety. The electrochemical performance of the *in-situ* Zn/MnO_2 cells could be further improved by optimizing the surface properties of carbon black to control the MnO_2 deposition (morphology, porosity, composition, loading mass, etc.) or by optimizing the electrolyte to improve the reversibility of the conversion reactions.

Conclusions

In this work, *in-situ* formed Zn/MnO_2 cells with Zn and carbon-black electrodes in $MnSO_4$-$ZnSO_4$ electrolyte are developed. Our coupled experimental and theoretical study clarifies the complex redox reactions in Zn/MnO_2 system, as such, there exists a concurrence of Zn^{2+} and H^+ intercalation and conversion reactions corresponding to the two discharge plateaus at ~ 1.40 V and ~ 1.26 V, respectively. These two types of reactions show distinct kinetics and thus distinct rate dependent capacities and capacity retention. The capacity of H^+/Zn^{2+} intercalation reactions is well retained and rate-insensitive while that of the subsequent H^+/Zn^{2+} conversion reactions is highly dependent on the discharge/charge rate. By virtue of the different rate-dependent electrochemical behavior for these two redox reactions, we successfully demonstrated ultra-high power and long-life Zn/MnO_2 cells which, after 1000 cycles, can still maintain an energy density of ~ 231 Wh kg^{-1} at a power density of ~ 4 kW kg^{-1} (9C, ~ 3.1 A g^{-1}) or an energy density of ~ 105 Wh kg^{-1} at a power density of ~ 15 kW kg^{-1} (30C, ~ 10.3 A g^{-1}). The excellent cycle stability and power capability are superior to most reported ZIBs with *ex-situ* MnO_2 or other cathode materials. In addition, the revealed reaction mechanisms in our *in-situ* Zn/MnO_2 cell could be applied to *ex-situ* Zn/MnO_2 systems or other ZIBs, opening an avenue to further improve their cycling and power performance. We therefore emphasize that through rationally control the active electrochemical reactions high power density and excellent cycle stability could be achieved in electrodes with multiple but kinetically different electrochemical redox reactions.

Conflicts of interest

There are no conflicts to declare.

Acknowledgements

This work is supported in part by the State of Washington through the University of Washington Clean Energy Institute and via funding from the Washington Research Foundation, and by Inamori Foundation. X-ray diffraction measurement is supported by General Motors, Research and Development. Soft X-ray spectroscopy was performed at the Advanced Light Source (ALS), which is a DOE Office of Science User Facility under contract no. DE-AC02-05CH11231.

Notes and references

1. Z. Yang, J. Zhang, M. C. Kintner-Meyer, X. Lu, D. Choi, J. P. Lemmon and J. Liu, *Chemical reviews*, 2011, **111**, 3577-3613.
2. B. Dunn, H. Kamath and J.-M. Tarascon, *Science*, 2011, **334**, 928-935.
3. H. Pan, Y. Shao, P. Yan, Y. Cheng, K. S. Han, Z. Nie, C. Wang, J. Yang, X. Li and P. Bhattacharya, *Nature Energy*, 2016, 16039.
4. J. B. Goodenough and Y. Kim, *Chemistry of Materials*, 2009, **22**, 587-603.
5. T. C. Wanger, *Conservation Letters*, 2011, **4**, 202-206.
6. M. Jacoby, *Chem. Eng. News*, 2013, **91**, 33-37.
7. E. P. Roth and C. J. Orendorff, *Electrochemical Society Interface*, 2012, **21**, 45-49.
8. D. H. Doughty, P. C. Butler, A. A. Akhil, N. H. Clark and J. D. Boyes, *The Electrochemical Society Interface*, 2010, **19**, 49-53.
9. T. Nguyen and R. F. Savinell, *The Electrochemical Society Interface*, 2010, **19**, 54-56.
10. M. Skyllas-Kazacos, M. Chakrabarti, S. Hajimolana, F. Mjalli and M. Saleem, *Journal of The Electrochemical Society*, 2011, **158**, R55-R79.
11. J. Sudworth and A. Tiley, *Sodium Sulphur Battery*, Springer Science & Business Media, 1985.
12. A. Bito, 2005.
13. M. Shiomi, T. Funato, K. Nakamura, K. Takahashi and M. Tsubota, *Journal of Power Sources*, 1997, **64**, 147-152.
14. L. Lam, N. Haigh, C. Phyland and A. Urban, *Journal of Power Sources*, 2004, **133**, 126-134.
15. W. Tang, Y. Zhu, Y. Hou, L. Liu, Y. Wu, K. P. Loh, H. Zhang and K. Zhu, *Energy & Environmental Science*, 2013, **6**, 2093-2104.
16. W. Li, J. R. Dahn and D. S. Wainwright, *Science*, 1994, **264**, 1115-1117.
17. J. Y. Luo and Y. Y. Xia, *Advanced Functional Materials*, 2007, **17**, 3877-3884.
18. J.-Y. Luo, W.-J. Cui, P. He and Y.-Y. Xia, *Nature chemistry*, 2010, **2**, 760-765.
19. Y. Lu, J. B. Goodenough and Y. Kim, *Journal of the American Chemical Society*, 2011, **133**, 5756-5759.
20. M. Pasta, C. D. Wessells, R. A. Huggins and Y. Cui, *Nature communications*, 2012, **3**, 1149.
21. S. Ha and K. T. Lee, *Nature Energy*, 2016, **1**, 16057.
22. C. D. Wessells, R. A. Huggins and Y. Cui, *Nature communications*, 2011, **2**, 550.
23. M.-C. Lin, M. Gong, B. Lu, Y. Wu, D.-Y. Wang, M. Guan, M. Angell, C. Chen, J. Yang and B.-J. Hwang, *Nature*, 2015, **520**, 324-328.
24. N. Zhang, F. Cheng, J. Liu, L. Wang, X. Long, X. Liu, F. Li and J. Chen, *Nature Communications*, 2017, **8**, 405.
25. N. D. Ingale, J. W. Gallaway, M. Nyce, A. Couzis and S. Banerjee, *Journal of Power Sources*, 2015, **276**, 7-18.
26. C. Wei, C. Xu, B. Li, H. Du and F. Kang, *Journal of Physics and Chemistry of Solids*, 2012, **73**, 1487-1491.
27. D. Xu, B. Li, C. Wei, Y.-B. He, H. Du, X. Chu, X. Qin, Q.-H. Yang and F. Kang, *Electrochimica Acta*, 2014, **133**, 254-261.

28. K. Kordesch, J. Gsellmann and K. Tomantschger, *Journal of Electroanalytical Chemistry and Interfacial Electrochemistry*, 1981, **118**, 187-201.
29. D. Qu, D. Diehl, B. Conway, W. Pell and S. Qian, *Journal of applied electrochemistry*, 2005, **35**, 1111-1120.
30. D. Qu, *Electrochemistry communications*, 2006, **8**, 1527-1530.
31. C. Mondoloni, M. Laborde, J. Rioux, E. Andoni and C. Lévy-Clément, *Journal of The Electrochemical Society*, 1992, **139**, 954-959.
32. A. Kozawa and J. Yeager, *Journal of The Electrochemical Society*, 1968, **115**, 1003-1007.
33. B. J. Hertzberg, A. Huang, A. Hsieh, M. Chamoun, G. Davies, J. K. Seo, Z. Zhong, M. Croft, C. Erdonmez and Y. S. Meng, *Chemistry of Materials*, 2016.
34. D. Qu, *Physical and electrochemical basis of induction of reversibility in manganese dioxide reduction and reoxidation*, University of Ottawa (Canada). 1994.
35. Y. F. Yao, N. Gupta and H. Wroblowa, *Journal of electroanalytical chemistry and interfacial electrochemistry*, 1987, **223**, 107-117.
36. H. Wroblowa and N. Gupta, *Journal of electroanalytical chemistry and interfacial electrochemistry*, 1987, **238**, 93-102.
37. L. Binder, K. Kordesch and P. Urdl, *Journal of The Electrochemical Society*, 1996, **143**, 13-17.
38. Y. Chabre and J. Pannetier, *Progress in Solid State Chemistry*, 1995, **23**, 1-130.
39. C. Xu, B. Li, H. Du and F. Kang, *Angewandte Chemie International Edition*, 2012, **51**, 933-935.
40. S. H. Kim and S. M. Oh, *Journal of power sources*, 1998, **72**, 150-158.
41. J. Lee, J. B. Ju, W. I. Cho, B. W. Cho and S. H. Oh, *Electrochimica Acta*, 2013, **112**, 138-143.
42. Z. Xiu, V. Mathew and J. Kim, *Electrochemistry Communications*, 2015, **60**, 121-125.
43. C. Xu, S. W. Chiang, J. Ma and F. Kang, *Journal of The Electrochemical Society*, 2013, **160**, A93-A97.
44. W. Sun, F. Wang, S. Hou, C. Yang, X. Fan, Z. Ma, T. Gao, F. Han, R. Hu, M. Zhu and C. Wang, *Journal of the American Chemical Society*, 2017, **139**, 9775-9778.
45. B. Lee, C. S. Yoon, H. R. Lee, K. Y. Chung, B. W. Cho and S. H. Oh, *Scientific reports*, 2014, **4**.
46. M. H. Alfaruqi, V. Mathew, J. Gim, S. Kim, J. Song, J. P. Baboo, S. H. Choi and J. Kim, *Chemistry of Materials*, 2015, **27**, 3609-3620.
47. T. Shoji and T. Yamamoto, *Journal of Electroanalytical Chemistry*, 1993, **362**, 153-157.
48. M. H. Alfaruqi, J. Gim, S. Kim, J. Song, J. Jo, S. Kim, V. Mathew and J. Kim, *Journal of Power Sources*, 2015, **288**, 0e327.
49. B. Lee, H. R. Lee, H. Kim, K. Y. Chung, B. W. Cho and S. H. Oh, *Chemical Communications*, 2015, **51**, 9265-9268.
50. D. A. Kitchaev, S. T. Dacek, W. Sun and G. Ceder, *Journal of the American Chemical Society*, 2017.
51. Y. Zhou, M. Toupin, D. Bélanger, T. Brousse and F. Favier, *Journal of Physics and Chemistry of Solids*, 2006, **67**, 1351-1354.
52. W. Wei, X. Cui, W. Chen and D. G. Ivey, *The Journal of Physical Chemistry C*, 2008, **112**, 15075-15083.
53. M. Narubayashi, Z. Chen, K. Hasegawa and S. Noda, *RSC Advances*, 2016, **6**, 41496-41505.
54. D. Qu, *Journal of power sources*, 2006, **156**, 692-699.
55. W.-H. Kao and V. Weibel, *Journal of applied electrochemistry*, 1992, **22**, 21-27.
56. J. P. Perdew, K. Burke and M. Ernzerhof, *Physical review letters*, 1996, **77**, 3865.
57. P. E. Blöchl, *Physical review B*, 1994, **50**, 17953.
58. G. Kresse and D. Joubert, *Physical Review B*, 1999, **59**, 1758.
59. G. Kresse and J. Hafner, *Physical Review B*, 1993, **47**, 558-561.
60. G. Kresse and J. Furthmüller, *Physical Review B*, 1996, **54**, 11169-11186.
61. J. Zaanen, O. Jepsen, O. Gunnarsson and A. Paxton, *Phys. Rev. B*, 1991, **44**, 943.
62. T. Mueller, G. Hautier, A. Jain and G. Ceder, *Chemistry of materials*, 2011, **23**, 3854-3862.
63. H. J. Monkhorst and J. D. Pack, *Physical review B*, 1976, **13**, 5188.
64. B. Lanson, V. A. Drits, E. Silvester and A. Manceau, *American Mineralogist*, 2000, **85**, 826-838.
65. E. Silvester, M. Manceau and V. A. Drits, *American Mineralogist*, 1997, **82**, 962-978.
66. A. Manceau, B. Lanson and V. A. Drits, *Geochimica et Cosmochimica Acta*, 2002, **66**, 2639-2663.
67. P. Ruetschi and R. Giovanoli, *Journal of The Electrochemical Society*, 1988, **135**, 2663-2669.
68. J. W. Gallaway, M. Menard, B. Hertzberg, Z. Zhong, M. Croft, L. A. Sviridov, D. E. Turney, S. Banerjee, D. A. Steingart and C. K. Erdonmez, *Journal of The Electrochemical Society*, 2015, **162**, A162-A168.
69. G. Lei, *Marine Geology*, 1996, **133**, 103-112.
70. R. Giovanoli, W. Feitknecht and F. Fischer, *Interim. Rept*, 1970.
71. W. Yang, X. Liu, R. Qiao, P. Olalde-Velasco, J. D. Spear, L. Roseguo, J. X. Pepper, J. D. Denlinger and Z. Hussain, *Journal of electron spectroscopy and related phenomena*, 2013, **190**, 64-74.
72. X. Liu, J. Liu, R. Qiao, Y. Yu, H. Li, L. Suo, Y.-s. Hu, Y.-D. Chuang, G. Shu and F. Chou, *Journal of the American Chemical Society*, 2012, **134**, 13708-13715.
73. R. Qiao, T. Chin, S. J. Harris, S. Yan and W. Yang, *Current Applied Physics*, 2013, **13**, 544-548.
74. R. Qiao, K. Dai, J. Mao, T.-C. Weng, D. Sokaras, D. Nordlund, X. Song, V. S. Battaglia, Z. Hussain and G. Liu, *Nano Energy*, 2015, **16**, 186-195.
75. Z. Zhuo, J. Hu, Y. Duan, W. Yang and F. Pan, *Applied Physics Letters*, 2016, **109**, 023901.
76. A. J. Bard, L. R. Faulkner, J. Leddy and C. G. Zoski, *Electrochemical methods: fundamentals and applications*, wiley New York, 1980.
77. X. Li, J. Liu, M. N. Banis, A. Lushington, R. Li, M. Cai and X. Sun, *Energy & Environmental Science*, 2014, **7**, 768-778.
78. M. H. Alfaruqi, S. Islam, J. Gim, J. Song, S. Kim, D. T. Pham, J. Jo, Z. Xiu, V. Mathew and J. Kim, *Chemical Physics Letters*, 2016, **650**, 64-68.
79. D. Kundu, B. D. Adams, V. Duffort, S. H. Vajargah and L. F. Nazar, *Nature Energy*, 2016, **1**, 16119.
80. B. Jiang, C. Xu, C. Wu, L. Dong, J. Li and F. Kang, *Electrochimica Acta*, 2017, **229**, 422-428.
81. J. Zhao, Y. Li, X. Peng, S. Dong, J. Ma, G. Cui and L. Chen, *Electrochemistry Communications*, 2016, **69**, 6-10.
82. L. Zhang, L. Chen, X. Zhou and Z. Liu, *Advanced Energy Materials*, 2015, **5**.
83. G. Li, Z. Yang, Y. Jiang, C. Jin, W. Huang, X. Ding and Y. Huang, *Nano Energy*, 2016, **25**, 211-217.
84. J. H. Jo, Y.-K. Sun and S.-T. Myung, *Journal of Materials Chemistry A*, 2017, **5**, 8367-8375.
85. Y. Zhang, K. Cheng, K. Ye, Y. Gao, W. Zhao, G. Wang and D. Cao, *Electrochimica Acta*, 2015, **182**, 971-978.
86. L. L. Zhang and X. Zhao, *Chemical Society Reviews*, 2009, **38**, 2520-2531.

Supplementary Information

Reaction mechanisms for long life and ultra-high power rechargeable Zn ion batteries

Yun Li,[a] Shanyu Wang,[a] James Salvador,[b] Jinpeng Wu,[c,d] Bo Liu,[e] Wanli Yang,[c] Jiong Yang,[e] Wenqing Zhang,[e] Jun Liu,[f] and Jihui Yang[a,*]

[a.] Material Science and Engineering Department, University of Washington, Seattle, WA 98195, USA.

[b.] Chemical Sciences and Materials Systems Lab, General Motors R&D Center, Warren, Michigan 48090, USA.

[c.] Advanced Light Source, Lawrence Berkeley National Laboratory, Berkeley, CA 94720, USA.

[d.] Geballe Laboratory for Advanced Materials, Stanford University, Stanford, CA 94305, USA.

[e.] Material Genome Institute, Shanghai University, 99 Shangda Road, Shanghai 200444, China.

[f.] Energy & Environment Directorate, Pacific Northwest National Laboratory, Richland, WA 99352, USA.

* Email: jihuiy@uw.edu

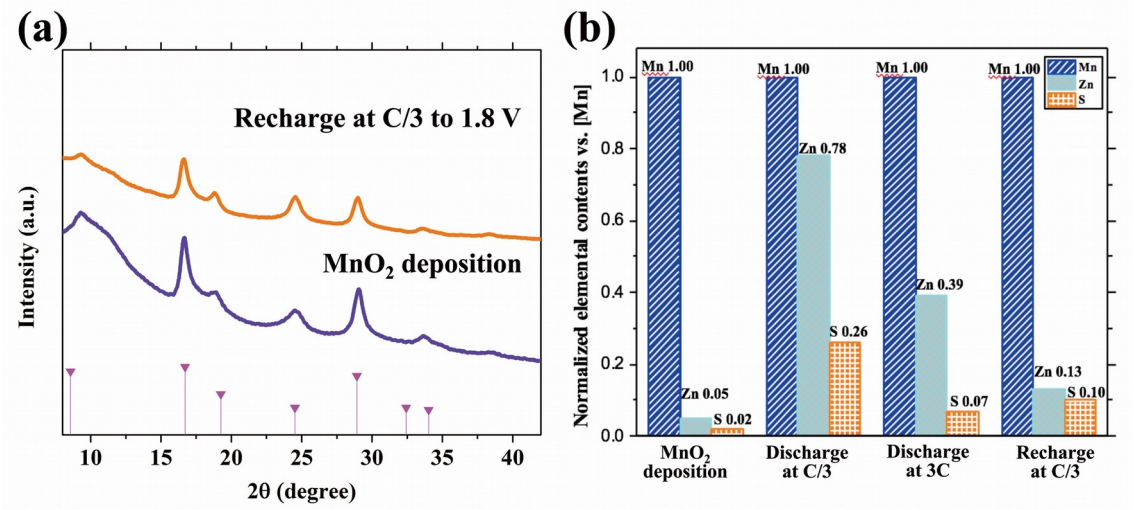

Fig. S1. (a) XRD patterns of the initially deposited MnO_2 and fully recharged cathodes at C/3. (b) The corresponding XRF analysis results of electrodes at different stages.

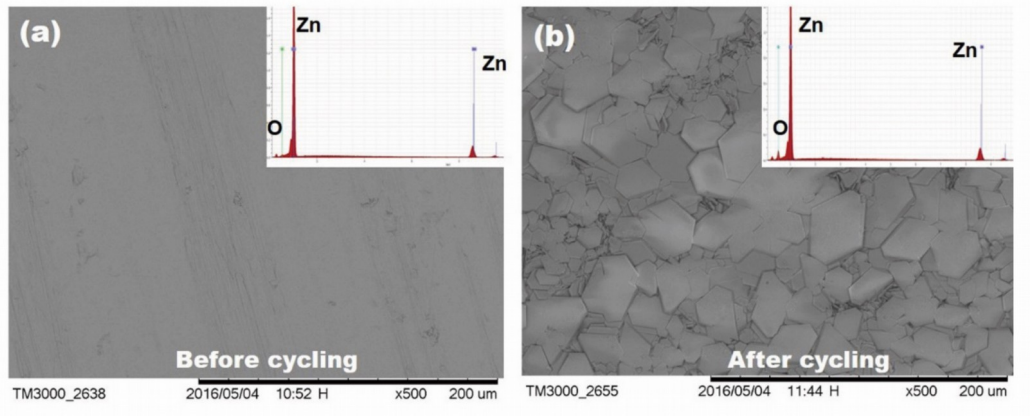

Fig. S2. SEM images of Zn anode (a) before and (b) after 20 cycles.

Table S1. The Gibbs free energies and resulting voltages of representative reaction equations.

Reaction Equations * Zn_xMnO_2 takes x=0.125 as an example	ΔG(eV)	Voltage(V)
1) $6MnO_2 + 3Zn + ZnSO_4 + 10H_2O \rightarrow 6MnOOH + ZnSO_4 \cdot 3Zn(OH)_2 \cdot 4H_2O$	-8.604	1.43
2) $8MnO_2 + Zn \rightarrow 8Zn_{0.125}MnO_2$ *	-2.009	1.01
3) $84MnO_2 + 33Zn + 10ZnSO_4 + 100H_2O \rightarrow 60MnOOH + 24Zn_{0.125}MnO_2 + 10[ZnSO_4 \cdot 3Zn(OH)_2 \cdot 4H_2O]$	-92.067	1.39
4) $18MnOOH + 3Zn + ZnSO_4 \rightarrow 6Mn_3O_4 + ZnSO_4 \cdot 3Zn(OH)_2 \cdot 4H_2O + 2H_2O$	-6.381	1.06
5) $6MnOOH + 3Zn + ZnSO_4 + 4H_2O \rightarrow 6MnO + ZnSO_4 \cdot 3Zn(OH)_2 \cdot 4H_2O$	-4.390	0.73
6) $72Zn_{0.125}MnO_2 + 39Zn + 16ZnSO_4 + 112H_2O \rightarrow 24Mn_3O_4 + 16[ZnSO_4 \cdot 3Zn(OH)_2 \cdot 4H_2O]$	-110.655	1.42
7) $24Zn_{0.125}MnO_2 + 21Zn + 8ZnSO_4 + 56H_2O \rightarrow 24MnO + 8[ZnSO_4 \cdot 3Zn(OH)_2 \cdot 4H_2O]$	-45.948	1.09
8) $8Zn_{0.125}MnO_2 + Zn + 4H_2O \rightarrow 2MnO + 2[ZnMn_3O_7 \cdot 2H_2O]$	-4.026	2.013
9) $8Zn_{0.125}MnO_2 + 16MnOOH + 4Zn + ZnSO_4 + 3H_2O \rightarrow 5Mn_3O_4 + 3MnO + 2[ZnMn_3O_7 \cdot 2H_2O] + ZnSO_4 \cdot 3Zn(OH)_2 \cdot 4H_2O$	-10.075	1.26
10) $48Zn_{0.125}MnO_2 + 74MnOOH + 41Zn + 10H_2O \rightarrow 38Mn_3O_4 + 8MnO + 47Zn(OH)_2$	-103.02	1.26